ARTICLE OPEN

Check for updates

# Quantum process tomography on holographic metasurfaces

Qing-Yuan Wu[1], Zhe Meng[1], Jia-Zhi Yang[1] and An-Ning Zhang[1]✉

Holographic metasurfaces and their applications have garnered significant attention owing to their role in polarization control. In this study, we demonstrate that the quantum properties of holographic metasurfaces can be obtained by quantum state tomography (QST) and quantum process tomography (QPT). We perform QST to obtain the experimental output states by extracting information from holograms encoded on the holographic metasurface, and develop a QPT-based method to estimate the quantum process of the metasurface. The theoretical output states derived from the estimated quantum process are in good agreement with the experimental output states, proving the effectiveness of our method. Our work not only provides theoretical and experimental analysis for understanding the quantum properties of holographic metasurfaces, but also paves the way for the application of holographic metasurfaces in quantum field.

*npj Quantum Information* (2022)8:46 ; https://doi.org/10.1038/s41534-022-00561-z

## INTRODUCTION

A metasurface comprises a structure whose period is shorter than the wavelength of the incident electromagnetic wave, and it can interact with waves on a subwavelength scale to control their responses. Altewischer et al. proved that the interaction between waves and metal nanostructures does not change the quantum properties of waves[1]. Therefore, metasurfaces have become an important platform for the development of quantum optics[2]. Wang et al. used a metasurface to achieve multiphoton interference[3], which is a strong proof that metasurfaces was used to manipulate quantum states. In recent years, researchers have used metasurfaces to realize classical coupling between photon spin and orbit[4], quantum entanglement between photon spin angular momentum and orbital angular momentum[5], long-distance quantum state manipulation[6–8], quantum coherence[9,10], preparation of quantum light sources[11–17], entanglement distillation[18,19], and dissipative-based quantum state control[20].

Holograms are an important tool for wavefront reconstruction, which can reconstruct the basic properties of waves, such as amplitude, phase, and polarization. The combination of a hologram and metasurface is considered a promising candidate in optics[21–27]. Researchers have studied polarization multiplexing holographic metasurfaces[28,29], but they can only provide multiplexing of two orthogonal polarization states, and there is strong crosstalk between the two information channels. Recently, Huang et al. proposed a metasurface that can realize multichannel vector holography[30]. A piece of this metasurface can achieve a high-fidelity, high-efficiency, wide-bandwidth hologram with a total of 12 polarization channels, and this provides the possibility for dynamic vectorial holographic display and triple protection for optical security. It further enhances the power of polarization control; however, its quantum properties are an unsolved mystery.

In this study, the holographic metasurface of reference[30] was used. We demonstrated that the quantum properties of holographic metasurfaces can be obtained by quantum state tomography (QST) and quantum process tomography (QPT). We constructed a 4f imaging system to reconstruct the holograms encoded on the metasurface. Thereafter, we extracted the information from the holograms and reconstructed the density matrices of the experimental output states using QST. Based on the results of QST, the quantum process of the holographic metasurface was estimated using QPT. Finally, we computed the theoretical output states to verify the effectiveness of the proposed method. We extract information from the holographic metasurface to perform QST and develop a QPT-based method to estimate the quantum process of the holographic metasurface. Our work not only proposes an alternative method to understand the quantum properties of holographic metasurfaces, but also paves the way for the application of holographic metasurfaces in the quantum field.

## RESULTS

### Principle of QST and QPT

QST is the procedure of experimentally determining an unknown quantum state. Suppose one qubit is encoded in the degree of polarization. We express the density matrix of the output state as follows:

$$\rho = \frac{T^{\dagger}T}{tr\left(T^{\dagger}T\right)} \tag{1}$$

where, $T$ denotes an arbitrary matrix. It can be proved that any matrix $T$ can ensure that $\rho$ satisfies the three requirements of the density matrix, namely Hermitian, positive semidefinite and normalization. We express $T$ in a lower triangular form for simplicity as follows:

$$T = \begin{bmatrix} t_1 & 0 \\ t_3 + \mathrm{i}t_4 & t_2 \end{bmatrix} \tag{2}$$

where $t_1, t_2, t_3$, and $t_4$ are four real parameters to be determined, and i is an imaginary unit.

When the state is observed at $\rho(t_1, t_2, t_3, t_4)$, and the noise is assumed to be a Gaussian distribution, the likelihood function $\mathcal{L}(t_1, t_2, t_3, t_4)$ representing the total probability can be expressed

[1]Center for Quantum Technology Research and Key Laboratory of Advanced Optoelectronic Quantum Architecture and Measurements (MOE), School of Physics, Beijing Institute of Technology, Beijing 100081, China. ✉email: Anningzhang@bit.edu.cn

as follows:

$$\mathcal{L}(t_1,t_2,t_3,t_4)=\frac{1}{A}\prod_i \exp-\frac{(n_i-\overline{n_i})^2}{2\sigma_i^2} \tag{3}$$

where $A$ denotes a normalization constant, $n_i$ is the value of the $i$th measurement, $\overline{n_i}=N\langle\psi_i|\rho|\psi_i\rangle$ is the expected value of the $i$th measurement, and $\sigma_i\approx\sqrt{\overline{n_i}}$ is the standard deviation of the Gaussian distribution. The core idea of the maximum likelihood estimation method is to estimate the four parameters to maximize the value of the likelihood function, and thus we obtain the following formula:

$$t_1,t_2,t_3,t_4=\arg\max\frac{1}{A}\prod_i \exp\left(-\frac{(n_i-N\langle\phi_i|\rho(t_1,t_2,t_3,t_4)|\phi_i\rangle)^2}{2N\langle\phi_i|\rho(t_1,t_2,t_3,t_4)|\phi_i\rangle}\right) \tag{4}$$

Finally, the density matrices of the output states were reconstructed using the four parameters. The quantum process of a holographic metasurface can be estimated using the output states. The procedure is described below.

The quantum process of the holographic metasurface is expressed as follows:

$$\varepsilon(\rho)=\sum_{i=0}^{3}E_i\rho E_i^\dagger \tag{5}$$

where $\varepsilon$ represents the quantum operation, $\varepsilon(\rho)$ is the output state, $\{E_i\}$ are the operation elements, and $\rho$ is the density matrix of the input states. The Pauli and identity matrices can form a fixed set, which is the basis for operators in the state space. Therefore, the operation elements can be expressed as follows:

$$E_i=\sum_m e_{im}\tilde{E}_m \tag{6}$$

where $\tilde{E}_0=I,\tilde{E}_1=\sigma_x,\tilde{E}_2=-i\sigma_y$, and $\tilde{E}_3=\sigma_z$. Then, Eq. (5) is equivalently expressed as follows:

$$\varepsilon(\rho)=\sum_{m,n=0}^{3}\tilde{E}_m\rho\tilde{E}_n^\dagger\chi_{mn} \tag{7}$$

where $\chi_{mn}=\sum_i e_{im}e_{in}^*$ represents a matrix of the superposition coefficients. Eq. (7) implies that if we determine $\chi_{mn}$, we have determined the operation elements $\{E_i\}$.

The four input states $|H\rangle$(horizontal polarization), $|V\rangle$(vertical polarization), $|D\rangle$(diagonal polarization), and $|L\rangle$(left-handed circular polarization) form a complete basis. Consequently, any output state $\varepsilon(\rho)$ can be expressed as a linear superposition of these four states as follows:

$$\varepsilon(\rho_j)=\sum_k\lambda_{jk}\rho_k \tag{8}$$

where $\lambda_{jk}$ denotes the superposition coefficient, $\rho_1=\rho_H,\rho_2=\rho_V$, $\rho_3=\rho_D$, and $\rho_4=\rho_L$. In Eq. (8), the output state $\varepsilon(\rho_j)$ is known from the QST, and $\rho_k$ is the density matrix of the input state; thus $\lambda_{jk}$ can be determined by linear algebra operations. Further, we assume the following linear relationship:

$$\tilde{E}_m\rho_j\tilde{E}_n^\dagger=\sum_{k=0}^{3}\beta_{jk}^{mn}\rho_k \tag{9}$$

where $\beta_{jk}^{mn}$ represents a matrix of superposition coefficients. After substituting $\{\tilde{E}_i\}$ and the density matrices of the input states into Eq. (9), we obtain $\beta_{jk}^{mn}$ by performing linear algebra operations.

Substituting Eq. (8) into Eq. (7), we obtain:

$$\sum_{m,n=0}^{3}\tilde{E}_m\rho_j\tilde{E}_n^\dagger\chi_{mn}=\sum_k\lambda_{jk}\rho_k \tag{10}$$

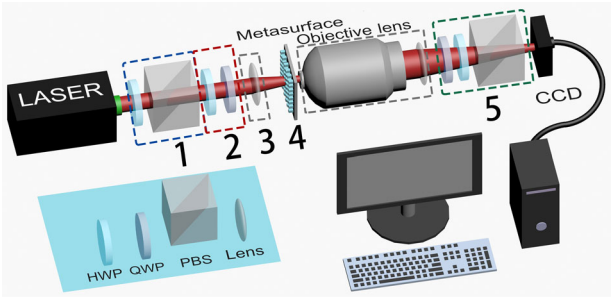


**Fig. 1 Experimental setup.** HWP1 and PBS1 were used to adjust the light intensity. The input states were generated by HWP2 and QWP1. Two lenses and an objective lens form the imaging system to reconstruct the hologram encoded on the metasurface. Measurement bases were generated using QWP2, HWP3, and PBS2.

Substituting Eq. (9) into Eq. (10), and each input state is independent of each other, the following formula is obtained:

$$\sum_{m,n=0}^{3}\chi_{mn}\beta_{jk}^{mn}=\lambda_{jk} \tag{11}$$

$\lambda_{jk}$ was determined using Eq. (8), whereas $\beta_{jk}^{mn}$ was determined using Eq. (9); thereafter we determine $\chi_{mn}$. Finally, the operation elements $\{E_i\}$ of the quantum process can be obtained using the following formula:

$$E_i=\sqrt{d_i}\sum_{j=0}^{3}U_{ji}\sigma_j \tag{12}$$

where $\chi_{mn}=\sum_{xy}U_{mx}d_x\delta_{xy}U_{ny}^*$

## Experimental results of QST and QPT on holographic metasurface

The experimental setup is illustrated in Fig. 1. In our experiment, an 810-nm laser is used as the light source. The experimental setup consists of five parts: the first part is used to adjust the light intensity, and this part contains a half-wave plate (HWP1) and polarizing beam splitter (PBS1); the second part, which contains HWP2 and a quarter wave plate (QWP1), is used to prepare the input states; the third part is a 4f imaging system, which contains two lenses and an objective lens; the fourth part is the holographic metasurface to be estimated; the fifth part is used to set the measurement bases, and this part contains QWP2, HWP3 and PBS2. Finally, a CCD is used to collect holograms.

The 4f imaging system adjusts the spot size of the laser to match the size of the holographic metasurface. Figure 2 shows the holograms collected by the CCD. Each hologram can be divided into two parts: the bright spot in the middle is the center point, and the three small figures around it are target images. The center point contains most of the laser energy; thus, it is the brightest part of the hologram. Furthermore, the hologram generated by the metasurface changes through the combination of different input states and measurement bases, and this change is clearest when the input state and measurement basis are orthogonal. Notably, our results are similar to those in reference[30], but we used more combinations to achieve QST and QPT.

Based on the information extracted from the holograms, the density matrices of the experimental output states were obtained using QST with maximum likelihood estimation. Six measurements are performed for each input state to ensure the accuracy of the estimation. Figure 3a shows the density matrices of the

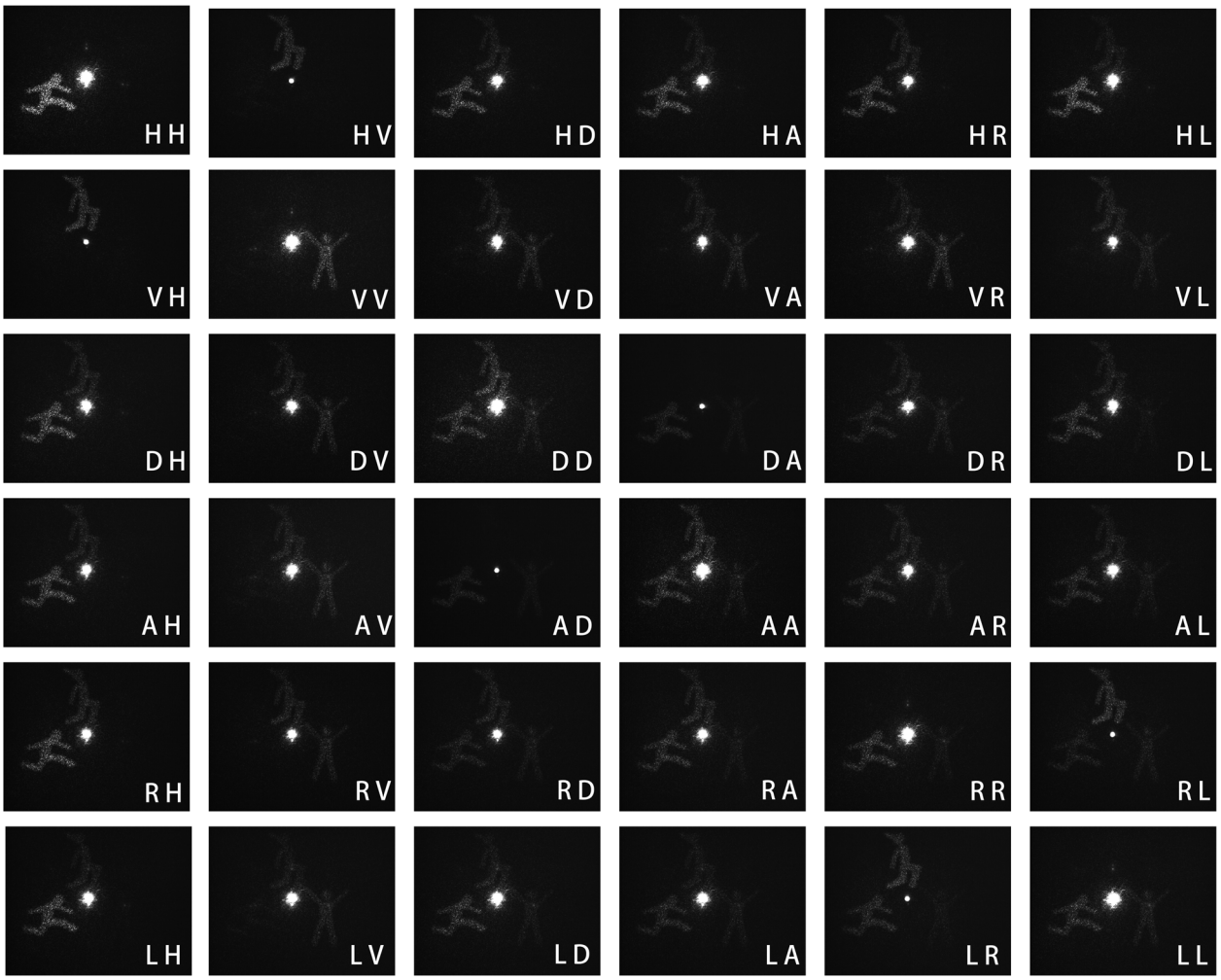


**Fig. 2 Results in CCD.** Six input states and six measurement bases were generated by changing the angles of Part2 and Part5. There are two letters in the lower-right corner of each graph; the former represents the input state, whereas the latter represents the measurement basis. The letters represent horizontal polarization ($|H\rangle$), vertical polarization ($|V\rangle$), diagonal polarization ($|D\rangle$), anti-diagonal polarization ($|A\rangle$), right-handed circular polarization ($|R\rangle$), and left-handed circular polarization ($|L\rangle$).

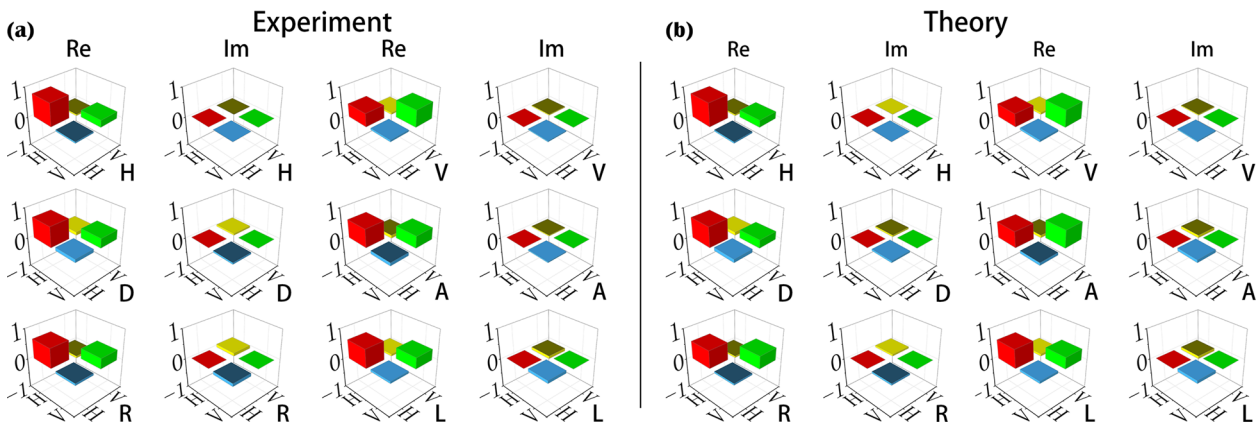


**Fig. 3 Density matrices of the experimental and theoretical output states.** The letters at the lower right corner indicate the input states. **a** This shows the density matrices of the experimental output states, which are estimated by QST; **b** It shows the density matrices of the theoretical output states, which are calculated from the results of QPT and the input states. The first and third columns represent the real part, and the second and fourth columns represent the imaginary part. The red, yellow, blue, and green columns indicate the components $|H\rangle\langle H|$, $|H\rangle\langle V|$, $|V\rangle\langle H|$, and $|V\rangle\langle V|$ of the density matrix, respectively.

experimental output states. From the figure, we observe that the $|H\rangle\langle H|$ and $|V\rangle\langle V|$ components are greater than zero in the real part of each density matrix. This indicates that the output states are superpositions of horizontal and vertical polarization states. The superposition of horizontal and vertical polarization states can also linearly represent other polarization states; thus, the holographic metasurface can achieve 12 channels multiplexing.

Based on our proposed QPT-based method, the quantum process of a holographic metasurface was estimated. We compute the density matrices of the theoretical output states using the results of the QPT and the input states. The results of computation are shown in Fig. 3b. The components of the density matrices of the experimental and theoretical output states are compared, as shown in Fig. 4, which serves as a criterion for evaluating the quantum process estimated by QPT. The comparison shows the difference between the density matrices of the experimental (Fig. 3a) and theoretical (Fig. 3b) output states. Not only the theoretical output states of the four states ($|H\rangle, |V\rangle, |D\rangle$, and $|L\rangle$) participating in the estimation of the quantum process, but also the theoretical output states of the two states ($|A\rangle$ and $|R\rangle$) not participating in the estimation match the experimental results. This indicates the effectiveness of our QPT-based method on a holographic metasurface.

## DISCUSSION

We demonstrate that QST and QPT can be used to estimate the quantum properties of a holographic metasurface. The quantum properties of multi-polarization multiplexed holographic metasurfaces were also investigated in this study. Our holographic metasurface encodes information in holograms containing the center point and target image. The center point, with no information, contains most of the laser energy, whereas the target image has all the information. Therefore, we can ignore the center point, which easily causes signal overflow and focuses only on the target image of all information encoding. This makes our method better than using all photons to perform QST in the case of signal overflow. The density matrices of the output states are obtained by QST. The calculation results demonstrate that the purity of each density matrix is: $|H\rangle : 0.51, |V\rangle : 0.505, |D\rangle : 0.837, |A\rangle : 0.512, |R\rangle : 0.501$, and $|L\rangle : 0.503$. Because $\rho(t) = U\rho(0)U^{\dagger}$ is only suitable for estimating quantum processes with pure output states, we develop a QPT-based method to address this challenge. The good agreement between the theoretical and experimental output states demonstrates the effectiveness of our method. Furthermore, the output states are not pure, indicating that our holographic metasurface is not a linear device. In the case of a single qubit, a linear device is generally represented by a two-dimensional matrix, whereas our holographic metasurface requires four two-dimensional matrices to describe its properties. Overall, the application of QST and QPT to holographic metasurfaces will pave the way for the application of holographic metasurfaces in the quantum field.

## METHODS

### Matrix of $\beta$

Let us rewrite Eq. (9) as follows:

$$\tilde{E}_m \rho_j \tilde{E}_n^{\dagger} = \sum_{k=0}^{3} \beta_{jk}^{mn} \rho_k \tag{13}$$

where, $\tilde{E}_0 = I, \tilde{E}_1 = \sigma_x, \tilde{E}_2 = -i\sigma_y, \tilde{E}_3 = \sigma_z$, $\rho_1 = \rho_H, \rho_2 = \rho_V, \rho_3 = \rho_D$ and $\rho_4 = \rho_L$. Using linear algebra operations, $\beta_{jk}^{mn}$ is obtained as follows:

$$\beta = \begin{bmatrix}
1 & -\frac{1+i}{2} & -\frac{1+i}{2} & 1 & -\frac{1-i}{2} & 0 & 0 & -\frac{1-i}{2} & -\frac{1-i}{2} & 0 & 0 & -\frac{1-i}{2} & 1 & -\frac{1-i}{2} & -\frac{1-i}{2} & 1 \\
0 & -\frac{1-i}{2} & -\frac{1-i}{2} & 0 & -\frac{1-i}{2} & 1 & 1 & -\frac{1-i}{2} & -\frac{1-i}{2} & 1 & 1 & -\frac{1-i}{2} & 0 & -\frac{1+i}{2} & -\frac{1+i}{2} & 0 \\
0 & 1 & 1 & 0 & 1 & 0 & 0 & 1 & 1 & 0 & 0 & 1 & 0 & 1 & 1 & 0 \\
0 & i & i & 0 & -i & 0 & 0 & -i & -i & 0 & 0 & -i & 0 & i & i & 0 \\
0 & -\frac{1-i}{2} & \frac{1-i}{2} & 0 & -\frac{1+i}{2} & 1 & -1 & \frac{1+i}{2} & \frac{1+i}{2} & -1 & 1 & -\frac{1+i}{2} & 0 & \frac{1-i}{2} & -\frac{1-i}{2} & 0 \\
1 & -\frac{1-i}{2} & \frac{1-i}{2} & -1 & -\frac{1+i}{2} & 0 & 0 & 1/2\,\frac{1+i}{2} & \frac{1+i}{2} & 0 & 0 & -\frac{1+i}{2} & -1 & \frac{1-i}{2} & -\frac{1-i}{2} & 1 \\
0 & 1 & -1 & 0 & 1 & 0 & 0 & -1 & -1 & 0 & 0 & 1 & 0 & -1 & 1 & 0 \\
0 & -i & i & 0 & i & 0 & 0 & -i & -i & 0 & 0 & i & 0 & i & -i & 0 \\
0 & 0 & -\frac{1+i}{2} & \frac{1+i}{2} & 0 & 0 & -\frac{1+i}{2} & \frac{1+i}{2} & -\frac{1-i}{2} & -\frac{1-i}{2} & 1 & -1 & \frac{1-i}{2} & \frac{1-i}{2} & -1 & 1 \\
0 & 0 & \frac{1-i}{2} & -\frac{1-i}{2} & 0 & 0 & -\frac{1+i}{2} & -\frac{1-i}{2} & \frac{1+i}{2} & \frac{1+i}{2} & 1 & -1 & -\frac{1+i}{2} & -\frac{1+i}{2} & -1 & 1 \\
1 & 1 & 0 & 0 & 1 & 1 & 0 & 0 & 0 & 0 & -1 & 1 & 0 & 0 & 1 & -1 \\
0 & 0 & i & -i & 0 & 0 & i & -i & -i & -i & 0 & 0 & i & i & 0 & 0 \\
0 & -\frac{1+i}{2} & 0 & \frac{1-i}{2} & -\frac{1-i}{2} & 1 & -\frac{1+i}{2} & i & 0 & -\frac{1-i}{2} & 0 & -\frac{1+i}{2} & \frac{1+i}{2} & -i & -\frac{1-i}{2} & 1 \\
0 & -\frac{1-i}{2} & 0 & -\frac{1+i}{2} & -\frac{1+i}{2} & 1 & \frac{1-i}{2} & i & 0 & \frac{1+i}{2} & 0 & -\frac{1-i}{2} & -\frac{1-i}{2} & -i & -\frac{1+i}{2} & 1 \\
0 & 1 & 0 & i & 1 & 0 & i & 0 & 0 & -i & 0 & 1 & -i & 0 & 1 & 0 \\
1 & 0 & i & 0 & 0 & -1 & 0 & -i & -i & 0 & 1 & 0 & 0 & i & 0 & -1
\end{bmatrix} \tag{14}$$

### Details of experiment

Based on the density matrices of the output states, the value of $\lambda$ was computed using Eq. (8), which is expressed as follows:

$$\lambda^T = [0.8110 \quad 0.2770 \quad -0.0952 \quad 0.0071 \quad 0.3508 \quad 0.4748 \quad 0.1118 \quad 0.0626 \quad 0.6273 \quad 0.2653 \quad 0.5160 \quad -0.1086 \quad 0.4711 \quad 0.2111 \quad 0.1318 \quad 0.1860] \tag{15}$$

Substituting Eq. (14) and Eq. (15) into Eq. (11), we obtain $\chi$:

$$\chi = \begin{bmatrix}
0.3177 & 0.0022 - i0.0086 & -0.0119 - i0.0018 & 0.0127 - i0.0074 \\
0.0022 + i0.0070 & 0.02676 & -0.0128 - i0.0032 & -0.0020 + i0.0018 \\
-0.0119 + i0.0002 & -0.0128 + i0.0032 & 0.1579 & 0.0086 + i0.0141 \\
0.0127 + i0.0074 & -0.0020 - i0.0002 & 0.0086 - i0.0125 & 0.2568
\end{bmatrix} \tag{16}$$

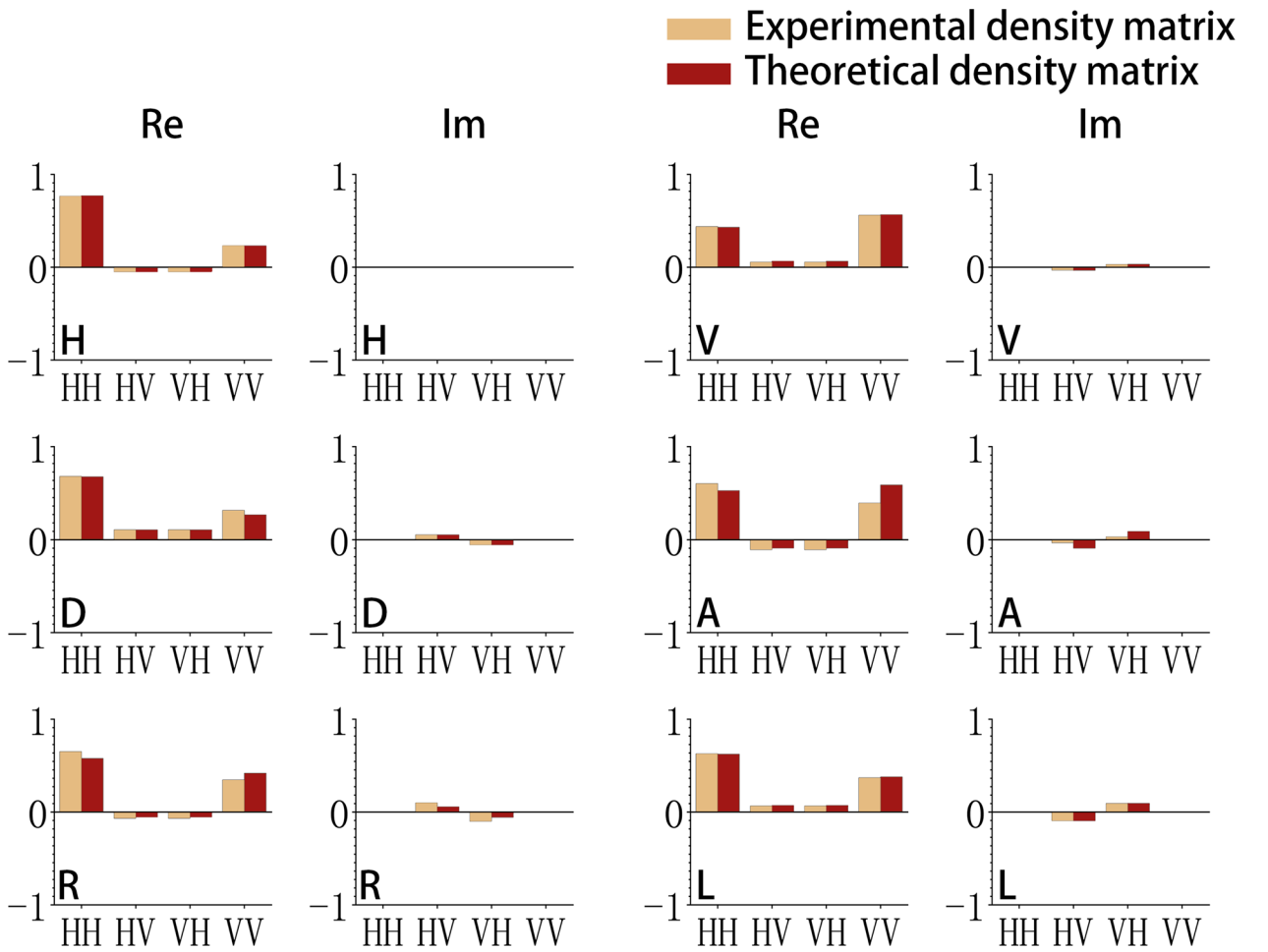


**Fig. 4 Comparison of the theoretical and experimental density matrices.** The first and third columns represent the real part, and the second and fourth columns represent the imaginary part. The experimental density matrix refers to the density matrix of the experimental output state, which is represented by orange bars. The theoretical density matrix refers to the density matrix of the theoretical output state, which is represented by red bars. The letters at the lower left corner indicate the input states. The theoretical output states of the four states( $|H\rangle, |V\rangle, |D\rangle$, and $|L\rangle$) involved in the estimation of the quantum process match the experimental results, and the theoretical output states of the two states($|A\rangle$ and $|R\rangle$) not involved in the estimation also match the experimental results. HH, HV, VH, and VV at the bottom of each graph represent the components of the density matrix.

Substituting Eq. (16) into Eq. (12), we obtain the operation elements $\{E_i\}$ of the holographic metasurface as follows:

$$E_0 = \begin{bmatrix} -0.0067 + i0.0456 & -0.3414 + i0.0107 \\ 0.4263 + i0.01 & 0.0613 - i0.0432 \end{bmatrix} \quad (17)$$

$$E_1 = \begin{bmatrix} 0.6191 + i0.0681 & 0.0698 + i0.0626 \\ -0.0171 + i0.0781 & 0.4477 - i0.0679 \end{bmatrix} \quad (18)$$

$$E_2 = \begin{bmatrix} 0.3597 + i0.0823 & 0.1113 - i0.0114 \\ 0.1767 + i0.0999 & -0.5586 + i0.0813 \end{bmatrix} \quad (19)$$

$$E_3 = \begin{bmatrix} -0.1746 + i0.1215 & 0.5542 + i0.0034 \\ 0.3999 - i0.0041 & 0.1535 - i0.0562 \end{bmatrix} \quad (20)$$

## DATA AVAILABILITY

No data were generated or analyzed in the presented research.

Received: 30 September 2021; Accepted: 17 March 2022;
Published online: 28 April 2022

## REFERENCES

1. Altewischer, E., Van Exter, M. P. & Woerdman, J.P. Plasmon-assisted transmission of entangled photons. *Nature* **418**, 304–306 (2002).
2. Solntsev, A. S., Agarwal, G. S. & Kivshar, Y. S. Metasurfaces for quantum photonics. *Nat. Photonics* **15**, 327–336 (2021).
3. Wang, K. et al. Quantum metasurface for multiphoton interference and state reconstruction. *Science* **361**, 1104–1108 (2018).
4. Bliokh, K. Y. & Nori, F. Transverse and longitudinal angular momenta of light. *Phys. Rep.* **592**, 1–38 (2015).
5. Stav, T. et al. Quantum entanglement of the spin and orbital angular momentum of photons using metamaterials. *Science* **361**, 1101–1104 (2018).
6. Biehs, S. -A. & Agarwal, G. S. Qubit entanglement across "-near-zero media. *Phys. Rev. A* **96**, 022308 (2017).
7. Jha, P. K., Ni, X., Wu, C., Wang, Y. & Zhang, X. Metasurface-enabled remote quantum interference. *Phys. Rev. Lett.* **115**, 025501 (2015).
8. Jha, P. K. et al. Metasurface-mediated quantum entanglement. *ACS Photonics* **5**, 971–976 (2017).
9. Wan, W. et al. Time-reversed lasing and interferometric control of absorption. *Science* **331**, 889–892 (2011).
10. Lyons, A. et al. Coherent metamaterial absorption of two-photon states with 40% efficiency. *Phys. Rev. A* **99**, 011801 (2019).
11. Bao, Y. et al. On-demand spin-state manipulation of single-photon emission from quantum dot integrated with metasurface. *Sci. Adv.* **6**, eaba8761 (2020).

12. Liu, J. et al. A solid-state source of strongly entangled photon pairs with high brightness and indistinguishability. *Nat. Nanotechnol.* **14**, 586–593 (2019).
13. Proscia, N. V. et al. Near-deterministic activation of room-temperature quantum emitters in hexagonal boron nitride. *Optica* **5**, 1128–1134 (2018).
14. Marino, G. et al. Spontaneous photon-pair generation from a dielectric nanoantenna. *Optica* **6**, 1416–1422 (2019).
15. Okoth, C., Cavanna, A., Santiago-Cruz, T. & Chekhova, M. V. Microscale generation of entangled photons without momentum conservation. *Phys. Rev. Lett.* **123**, 263602 (2019).
16. Li, L. et al. Metalens-array-based high-dimensional and multiphoton quantum source. *Science* **368**, 1487–1490 (2020).
17. Ming, Y. et al. Photonic entanglement based on nonlinear metamaterials. *Laser Photonics Rev.* **14**, 1900146 (2020).
18. Asano, M. et al. Distillation of photon entanglement using a plasmonic metamaterial. *Sci. Rep.* **5**, 1–8 (2015).
19. Farooqui, Md Abdullah Al. et al. Quantum entanglement distillation with metamaterials. *Opt. Express* **23**, 17941–17954 (2015).
20. Roger, T. et al. Coherent perfect absorption in deeply subwavelength films in the single-photon regime. *Nat. Commun.* **6**, 1–5 (2015).
21. Zheng, G. et al. Metasurface holograms reaching 80% efficiency. *Nat. Nanotechnol.* **10**, 308–312 (2015).
22. Khorasaninejad, M., Ambrosio, A., Kanhaiya, P. & Capasso, F. Broadband and chiral binary dielectric meta-holograms. *Sci. Adv.* **2**, e1501258 (2016).
23. Devlin, R. C., Khorasaninejad, M., Chen, W. T., Oh, J. & Capasso, F. Broadband high-efficiency dielectric metasurfaces for the visible spectrum. *Proc. Natl Acad. Sci.* **113**, 10473–10478 (2016).
24. Ni, X., Kildishev, A. V. & Shalaev, V. M. Metasurface holograms for visible light. *Nat. Commun.* **4**, 1–6 (2013).
25. Lee, G.-Y. et al. Complete amplitude and phase control of light using broadband holographic metasurfaces. *Nanoscale* **10**, 4237–4245 (2018).
26. Xu, Q. et al. Polarization-controlled surface plasmon holography. *Laser Photonics Rev.* **11**, 1600212 (2017).
27. Zhang, C. et al. Multichannel metasurface for simultaneous control of holograms and twisted light beams. *ACS Photonics* **4**, 1906–1912 (2017).
28. Montelongo, Y., Tenorio-Pearl, J. O., Milne, W. I. & Wilkinson, T. D. Polarization switchable diffraction based on subwavelength plasmonic nanoantennas. *Nano Lett.* **14**, 294–298 (2014).
29. Wen, D. et al. Helicity multiplexed broadband metasurface holograms. *Nat. Commun.* **6**, 1–7 (2015).
30. Zhao, R. et al. Multichannel vectorial holographic display and encryption. *Light. Sci. Appl.* **7**, 1–9 (2018).

## ACKNOWLEDGEMENTS

This work is supported by National Key Research and Development Program Earth Observation and Navigation Key Specialities (No. 2018YFB0504300). The authors thank Prof. Ling-Ling Huang and Dr. Rui-Zhe Zhao.

## AUTHOR CONTRIBUTIONS

Q.-Y.W., Z.M., J.-Z. Yang performed the experiments. Q.-Y.W. evaluated the data. Q.-Y.W., Z.M., and A.-N.Z wrote the article. All authors contributed to the planning of the experiments and commented on the article. The project is supervised by Prof. A.-N.Z.

## COMPETING INTERESTS

The authors declare no competing interests.

## ADDITIONAL INFORMATION

**Correspondence** and requests for materials should be addressed to An-Ning Zhang.

**Reprints and permission information** is available at http://www.nature.com/reprints

**Publisher's note** Springer Nature remains neutral with regard to jurisdictional claims in published maps and institutional affiliations.